

Supporting information

Incorporation of Atomic Palladium in Manganese Oxide for Enhanced Electrocatalysis

Email of corresponding authors:

lixp@sari.ac.cn; sunyh@sari.ac.cn

Experimental

Materials: Chemicals used for preparation were of analytical grade (SinoPharm Co. Ltd.) and were used as received without further purification. Nafion solution (5 wt%) was obtained from Sigma Aldrich. Multi-walled CNT (Length ~ 50 μm , Purity > 95 wt.%, Ash < 1.5 wt.%) was received from XF Nano Nanjing Co. Ltd. and washed with 3 M H_2SO_4 at 60 $^\circ\text{C}$ to remove potential metal impurities. CNTs have diameters in the ranges of 8–15 nm, and a few can reach up to 30 nm based on TEM examination. 20 wt.%Pd/C, 20 wt.% Pt/C and PtRu/C were purchased from Johnson-Matthey.

Preparation of catalysts:

Un-doped $\alpha\text{-MnO}_2$: $\text{MnSO}_4 \cdot \text{H}_2\text{O}$ (0.845 g), $(\text{NH}_4)_2\text{S}_2\text{O}_8$ (1.141 g) and $(\text{NH}_4)_2\text{SO}_4$ (2.643 g) were mixed in ultrapure water (18 M Ω .cm, 20mL) at room temperature under vigorous magnetic stirring. The solution was then transferred into a 25 mL Teflon-lined stainless steel autoclave. The autoclave was heated at 140 $^\circ\text{C}$ for 12 h in the oven and then allowed to cool down to room temperature. The collected black precipitate was subjected to repeated washing (with a large amount of water) and dried at 120 $^\circ\text{C}$ overnight in the oven.

Pd/MnO₂: Preparation of the Pd/MnO₂ followed identical steps as the $\alpha\text{-MnO}_2$ except for adding 0.0435 g $\text{Pd}(\text{NO}_3)_2 \cdot 2\text{H}_2\text{O}$ in the mixed precursor solution.

Pd/MnO₂-CNT: Preparation of the Pd/MnO₂-CNT followed identical steps as the Pd/MnO₂ except for adding 0.16 g CNT in the mixed precursor solution.

Pd/CNT: Preparation of the Pd/CNT followed identical steps as the Pd/MnO₂-CNT except for removing MnSO₄ in the precursors.

Pd/CNT+MnO₂: 3.65 mg MnO₂ and 1.35 mg Pd/CNT were physically mixed together. The catalyst powder was then transferred into a clean glass bottle containing 750 μ L ultrapure, 250 μ L isopropyl alcohol and 45 μ L Nafion solution. The solution was then ultrasonicated for 30 min to generate homogenous catalyst ink for RDE test.

Pd/MnO₂+CNT: 3.65 mg Pd/MnO₂ and 1.35 mg CNT were physically mixed together. The following step is identical to that of Pd/CNT+MnO₂.

Material characterization:

X-ray diffraction (XRD) was performed on an Ultima IV diffractometer with Cu K α radiation ($\lambda=0.15418$ nm, Rigaku). The SXRD measurement was conducted at the beamline BL44B2 of SPring-8 (Hyogo, Japan). The powder sample was sealed in borosilicate glass capillaries in vacuum. The data was collected employing a Debye-Scherrer camera installed with an imaging plate as an X-ray detector. The incident wavelengths were 0.5003 Å. The calibration was done using CeO₂ as the standard sample. Transmission electron microscopy (TEM, FEI Tecnai G2) installed with energy dispersive spectrometer (EDS, Oxford) was used to investigate the microstructure and Pd loading amount. Sub-Ångström-resolution HAADF-STEM images were recorded on a JEOL ARM200F, equipped with a CEOS probe corrector and with a guaranteed resolution of 0.08 nm. The XPS spectra was collected on a Thermo Scientific K-Alpha XPS spectrometer using Al K α X-ray source. Calibration of binding energy was done by setting the binding energy of C1s peak to 284.8 eV. X-ray absorption spectroscopy (XAS) measurements were carried out on the Beam line BL14W1 at the Shanghai Synchrotron Radiation Facility (SSRF). The electron storage ring was conducted at 3.5 GeV, using a double Si (311) crystal monochromator. X-ray absorption data was acquired under fluorescence mode. Utilizing the ATHENA module of the IFEFFIT software packages, the obtained EXAFS data were

performed according to the standard procedures. The EXAFS contributions were separated from different coordination shells by using a hanning windows ($dk=1.0 \text{ \AA}^{-1}$). Subsequently, the quantitative curve-fittings were carried out in the R-space ($1.0-3.2 \text{ \AA}$) with a Fourier transform k-space range of $3.0-12.0 \text{ \AA}^{-1}$ using the module ARTEMIS of IFEFFIT. And all fits were performed in the R space with k -weight of 2. During the curve-fitting, the overall amplitude reduction factor S_0^2 was fixed to the best-fit value of 0.73 determined from fitting the data of metal Pd foil. The EXAFS R-factor that measures the percentage misfit of the theory to the data is used to evaluate the goodness of the fit. If the R-factor is small, then the fitted model is very similar to the data. Specially, R-factor is defined as:

$$R = \frac{\sum_{i=1}^N (data_i - fit_i)^2}{\sum_{i=1}^N (data_i)^2}$$

All raw data in k space weighted by 0 were extracted from Athena software, and during WT-analysis the data were weighted by 2. The original XAS data in k space were transformed based on Morlet wavelet by using the program developed by Funke et al.^[S3]. The resolution of WT contour plot in k or R was optimized by modulating Morlet parameters (κ and σ).

Electrocatalytic measurements: Electrochemical measurements were performed with a Princeton multichannel potentiostat (PARSTAT MC) at room temperature of ~25 °C. A three electrode configuration was applied using a Pt wire as the counter electrode and Ag/AgCl (Metrohm, 3M KCl) as the reference electrode, respectively. The catalyst ink was prepared by dispersing 5 mg of catalyst powder in 1 mL of 3:1 v/v water/isopropyl alcohol solution with the addition of 45 μ L of 5 wt.% Nafion solution (Sigma-Aldrich). The dispersion was then subjected to ultrasonication for at least 30 min to form homogeneous catalyst ink. The ORR performance was characterized using a rotating disk electrode (RDE, PINE, 5 mm diameter, 0.19625 cm²). The glassy carbon electrode was cleaned and polished to a mirror finish prior to use. 8 μ L of dispersion was transferred onto the glassy carbon disk and then dried at room temperature. The electrolyte was 0.1 M KOH aqueous solution constantly purged with a high-purity O₂ flow. The linear scan voltammograms (LSV) were measured with a scanning rate 10 mV s⁻¹ from 1.05 V to 0.15 V (vs. RHE) at rotating speeds ranging from 225 rpm to 2025 rpm.

Rotating ring disk electrode (RRDE) measurements were conducted to determine the electron transfer number (n) and peroxide yield. The disk diameter, ring inner diameter, and ring outer diameter of the RRDE (Pine Research Instrumentation, USA) are 5.61, 6.25, and 7.92 mm, respectively. The catalyst loading step was identical to that for RDE. The n could be calculated from the disk current (I_d) and ring current (I_r) by following equation:

$$n = 4 \frac{I_d}{I_d + I_r/N}$$

where N is the collection rate of the RRDE and the value is 0.37. Furthermore, the peroxide yield was calculated via the following equation:

$$H_2O_2 (\%) = 100 \frac{2I_r/N}{I_d + I_r/N}$$

The turnover frequency (TOF) (s^{-1}) was calculated following previous report^[S4]:

$$\text{TOF } (s^{-1}) = \frac{\text{number of oxygen turnover}(\text{cm}^2\text{geometric area})}{\text{the active sites } (\text{cm}^2\text{geometric area})} = \frac{\left(\frac{J}{4F}\right)}{n}$$

where J is the current density for ORR at a given overpotential; n is the number of active sites; F is the faraday constant (96500 C/mol). The background current density from supports were subtracted.

Number of Pd sites

$$n \left(\frac{1}{\text{cm}^2} \right) = \left(\text{mol of active Pd } \frac{1}{\text{cm}^2} \right) \times 6.02 \times 10^{23}$$

$$= \left(\frac{m_{\text{Pd}}}{M_{\text{Pd}}} \frac{1}{\text{cm}^2} \right) \times 6.02 \times 10^{23}$$

where m_{Pd} is the mass of loaded palladium calculated based on ICP-OES data; M_{Pd} is the molar mass of palladium.

Electrochemical impedance spectroscopy measurement was carried out by using ac amplitude of 10 mV with a frequency range of 100,000 to 0.1 Hz. The C_{dl} was obtained by recording CV curves at different scanning rates. The linear slope of capacitive current vs. scanning rate is equivalent to twice C_{dl} . The consecutive CV measurements were performed in the potential range of 0.60–1.74 V for examining the stability of the as-prepared catalysts continuously catalyzing OER and ORR. The catalyst was loaded the porous carbon fiber electrode with a mass loading of 1.0 mg cm^{-2} . The 6 M KOH electrolyte was rigorously treated to remove Fe impurities.

Aqueous Zn–air battery (ZAB) test

The conventional aqueous ZAB was assembled in a two-electrode configuration using polished Zn foil as the Zn source. The electrolyte was 6 M KOH aqueous solution. The air electrode was prepared by drop casting the homogeneous catalyst ink onto the porous carbon fiber paper (Toray, TGP-H-060) with a mass loading of 2 mg cm⁻². The ink was prepared by dispersing the catalyst powder (2 mg) in 400 μL of 3:1 v/v water/isopropyl alcohol solution mixed solvent with 45 μL of 5 wt.% Nafion solution. The reference PtRu/C based air electrode was also prepared in an identical way.

Flexible solid-state Zinc–air battery (SZAB) test

The PVA gel electrolyte was prepared by a phase inversion method. 5 g of polyvinyl alcohol polymer (PVA) (99%, SinoPharm Co. Ltd.) were fully dissolved in 95 g of ultrapure water under vigorous magnetic stirring for 60 min at 70 °C to form a homogeneous solution. After cooling down to room temperature, the 5 wt. % PVA solution was casted onto a glass mold to obtain a membrane. The PVA membrane was then immersed in a 6 M KOH solution for 24 h. The flexible ZAB was assembled in a layer by layer manner. Zn foil and air electrode were placed in a face-to-face configuration separated by the PVA membrane. The air electrode was prepared by drop casting the catalyst ink onto the conductive carbon cloth with a mass loading of 1 mg cm⁻².

DFT calculations

All spin-polarized DFT calculations were performed by using projector augmented wave (PAW)^[S5] potentials and the Perdew–Burke–Ernzerhof (PBE) functional^[S6] implemented in the Vienna ab initio simulation package (VASP).^[S7, S8] Meanwhile, PBEsol for exchange and

correlation were also used refer to MnO₂. The cutoff energy was set as 400eV. Total energies and electron densities were computed within the DFT +U approach of Dudarev et al.,^[S9] in which a $U_{\text{eff}} = 1.6$ eV was used in the present work, as reported in the literature.^[S10] MnO₂ (100) slab structure having four stoichiometric layers and a 1×2 surface supercell, separated by 15 Å of vacuum to minimize their interaction. Monkhorst-Pack grids^[S11] with $2 \times 4 \times 1$ k-point sampling were used for MnO₂ (100) surface. The Pd-doping carbon nanotube models were modeled by Pd-doping graphene as former theoretical study suggested that a reasonable computational result can be obtained by a considerable size of graphene cluster.^[S12] The graphene fragment models were set in rectangular supercells and armchair and zigzag edges consists of 5 benzene rings in width. The vacuum thickness between graphene layers was set as 13 Å to avoid interlayer interactions. A $5 \times 1 \times 1$ Monkhorst-Pack k-point sampling was used for all models. Several models of graphene fragments containing Pd atoms bonded with two oxygen atoms on the armchair or zigzag graphene edge or oxygen atoms pre-adsorbed with carbon neighbors. The energies and the forces were converged to within 10^{-4} eV per atom, 0.03 eV Å⁻¹, respectively. The interaction energy of a Pd-group metal atom with oxygen-doped graphene fragment was calculated as $E^{\text{int}} = E^{\text{tot}}(\text{fragment}) + E^{\text{tot}}(\text{Pd}) - E^{\text{tot}}(\text{model})$, where $E^{\text{tot}}(\text{fragment})$, $E^{\text{tot}}(\text{Pd})$ and $E^{\text{tot}}(\text{model})$ are the total energy of the isolated initial oxygen-doped graphene fragment, of the single Pd atom, and of the model, respectively. The O₂ adsorption energy E^{ads} was defined as $E_{\text{ads}} = E^{\text{tot}}(\text{O}_2\text{-model}) - E^{\text{tot}}(\text{O}_2\text{gas}) - E^{\text{tot}}(\text{model})$, where $E^{\text{tot}}(\text{O}_2\text{-model})$ is the energy with O₂ adsorbed on the model, $E^{\text{tot}}(\text{O}_2\text{gas})$ is the energy of gasphase O₂, and E^{tot} is the energy of the model. Calculations indicated that Pd-O/C had much higher E_{ads} (-1.86 eV – -3.02 eV) than Pd/MnO₂ ($E_{\text{ads}} = -0.80$ eV), and therefore O₂ molecule was assumed to be pre-adsorbed on the Pd-O/C. The adsorption free energy of OH* (ΔG_{OH^*}) was calculated following previous work.^[S13]

$$\Delta G_{\text{OH}^*} = \Delta G(\text{H}_2\text{O}(\text{g}) + * \rightarrow \text{OH}^* + 1/2\text{H}_2(\text{g}))$$

$$\begin{aligned}
&= \mu_{\text{OH}^*} + 0.5 \times \mu_{\text{H}_2} - \mu_{\text{H}_2\text{O}} - \mu_* \\
&= (E_{\text{OH}^*} + 0.5 \times E_{\text{H}_2} - E_{\text{H}_2\text{O}} - E_*) \\
&\quad + (E_{\text{ZPE}(\text{OH}^*)} + 0.5 \times E_{\text{ZPE}(\text{H}_2)} - E_{\text{ZPE}(\text{H}_2\text{O})} - E_{\text{ZPE}(\text{*})}) \\
&\quad - T \times (S_{\text{OH}^*} + 0.5 \times S_{\text{H}_2} - S_{\text{H}_2\text{O}} - S_*)
\end{aligned}$$

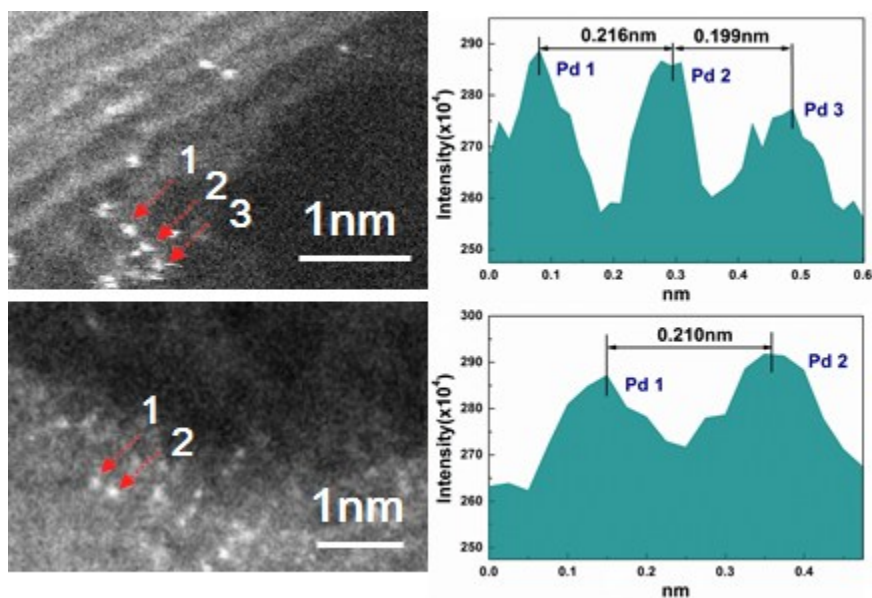


Figure S1. Sub-Ångström-resolution HAADF-STEM image of some Pd clusters supported by CNT. Note: The measured interatomic distances from STEM do not fully equal to that derived from EXAFS fitting, because the latter one is the macroscopically collected average information.

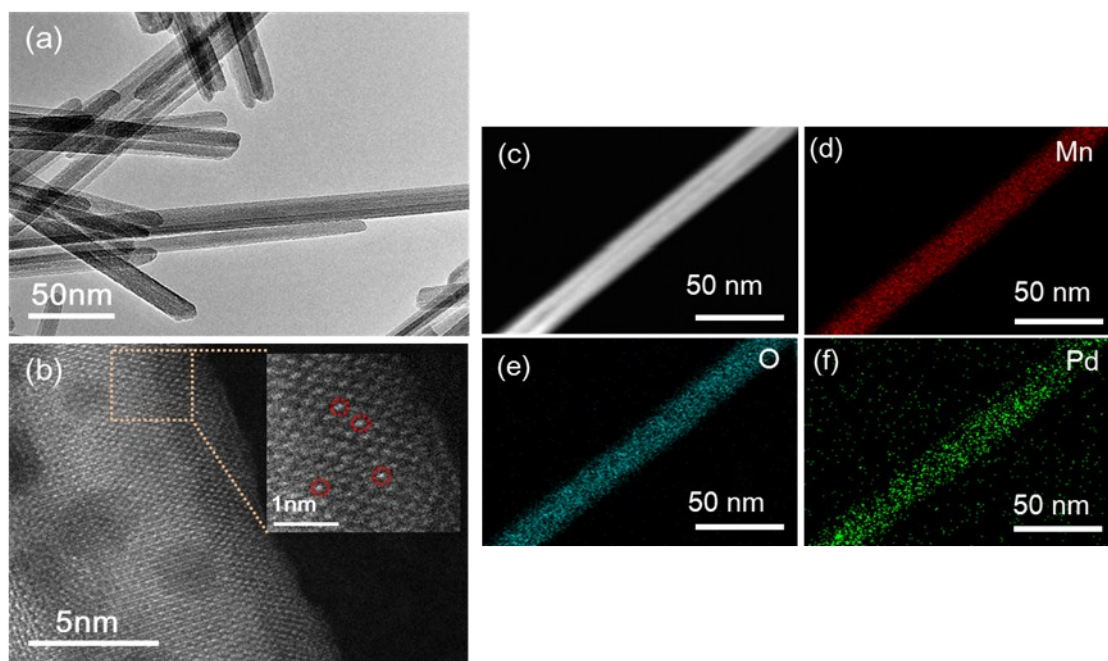


Figure S2. (a) TEM image and (b) sub-Ångström-resolution HAADF-STEM image of Pd/MnO₂. (c) STEM image and corresponding EDS element mapping of Pd/MnO₂.

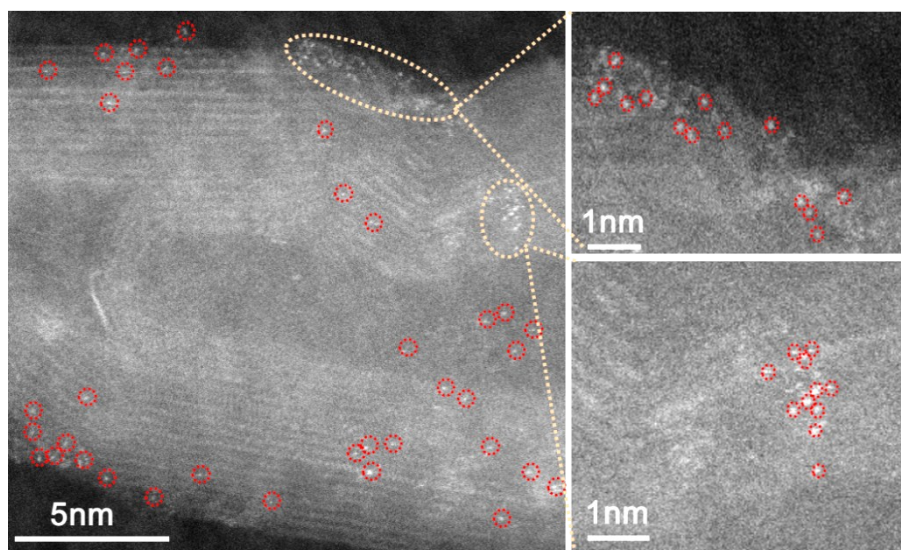


Figure S3. Sub-Ångström-resolution HAADF-STEM image of Pd/CNT.

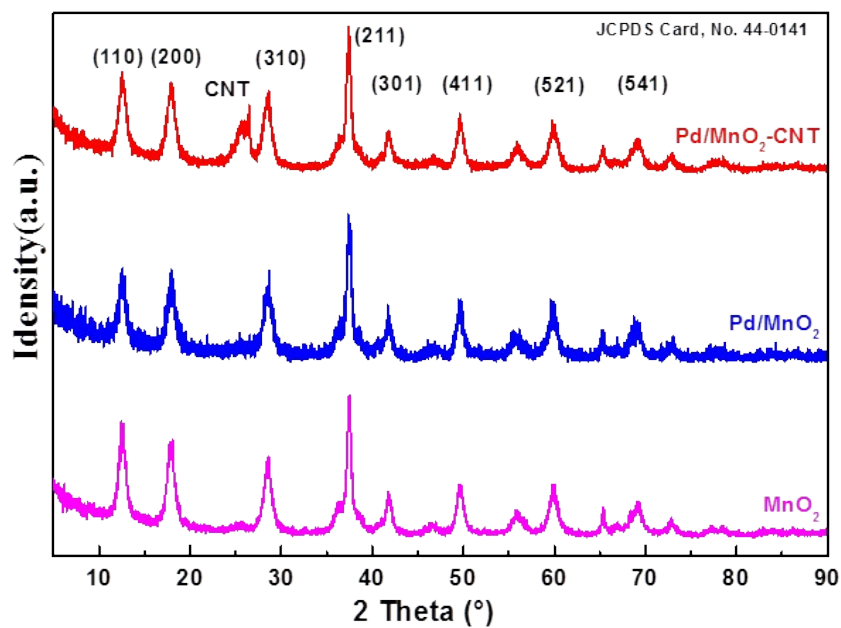


Figure S4. X-ray diffraction (XRD) pattern of MnO₂, Pd/MnO₂ and Pd/MnO₂-CNT.

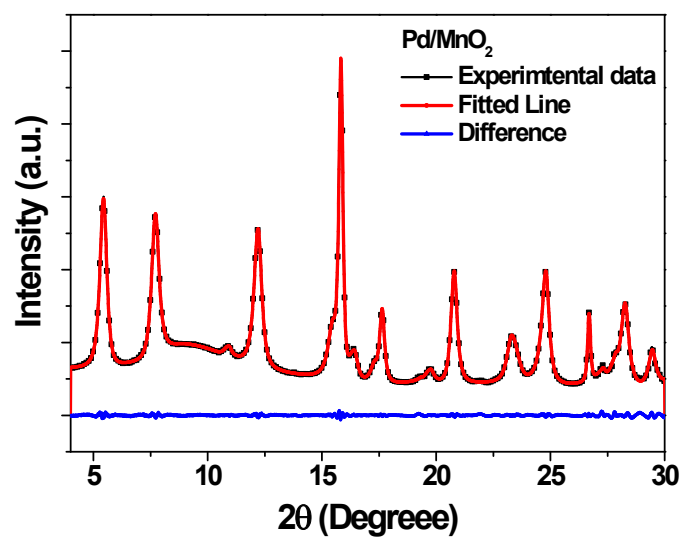


Figure S5. Synchrotron XRD pattern of Pd/MnO₂.

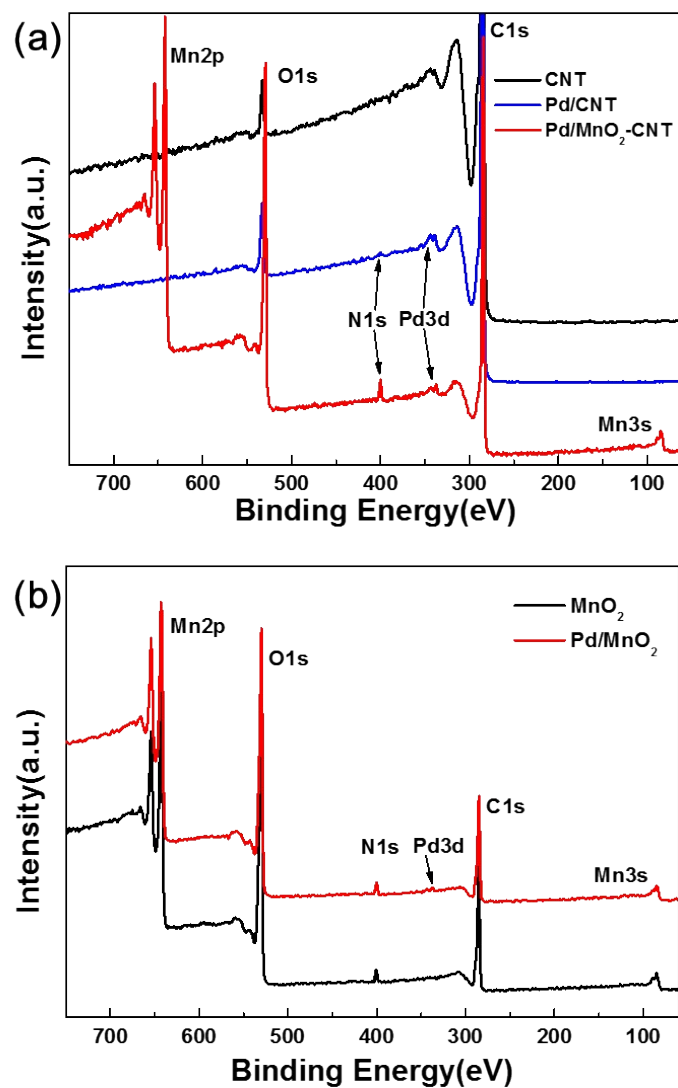


Figure S6. Wide-scan XPS survey spectra of (a) CNT, Pd/CNT and Pd/MnO₂-CNT, (b) MnO₂ and Pd/MnO₂.

Table S1. Element contents measured by XPS. The contents are all in weight percentage (wt.%). Note: HCl etching removes MnO₂ and Pd.

Element	CNT (%)	Pd/CNT (%)	Pd/MnO ₂ (%)	Pd/MnO ₂ -CNT (%)	Pd/MnO ₂ -CNT(HCl) (%)	Cycled Pd/MnO ₂ -CNT(HCl) (%)
O	2.73	5.15	24.90	16.22	4.37	7.57
N	--	0.67	1.57	1.15	0.63	0.73
C	97.27	92.54	--	38.86	95.00	91.70
Pd	--	1.64	0.67	0.89	--	--
Mn	--	--	72.86	42.88	--	--

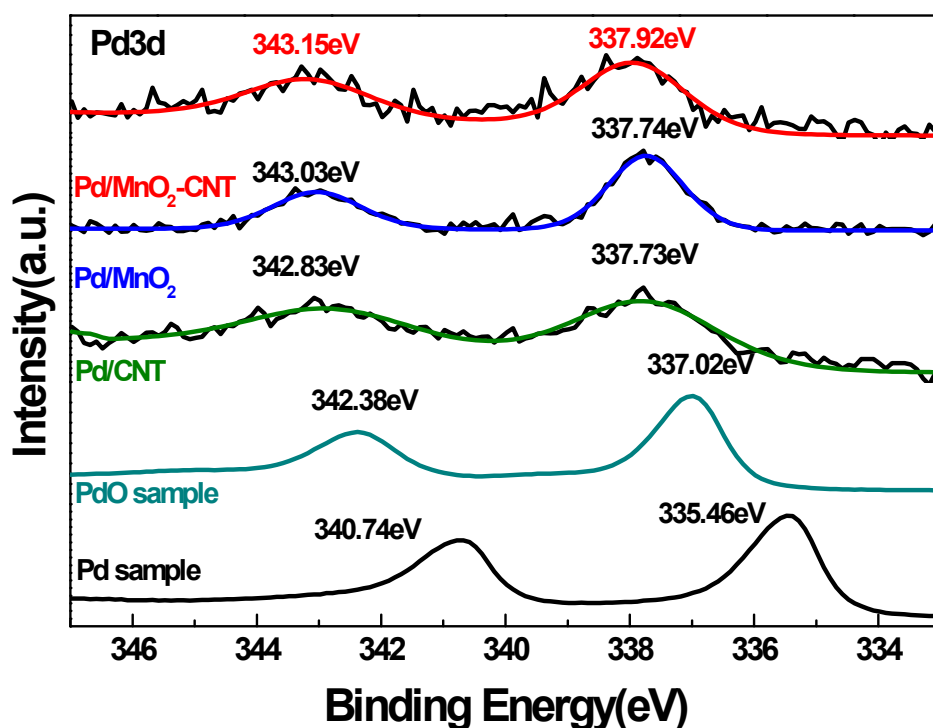


Figure S7. High resolution Pd 3d spectra of Pd/MnO₂-CNT, Pd/MnO₂, Pd/CNT, PdO and metallic Pd foil.

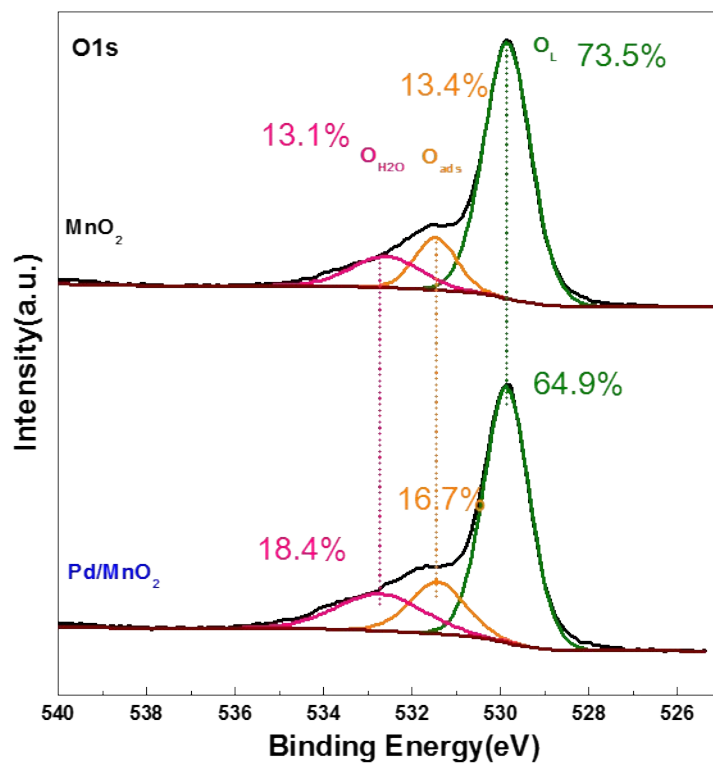


Figure S8. High resolution O1s spectra of MnO₂ and Pd/MnO₂. O_L, O_{ads} and O_{H2O} represent lattice oxygen surface, oxygen adsorption species and minor attached water, respectively.

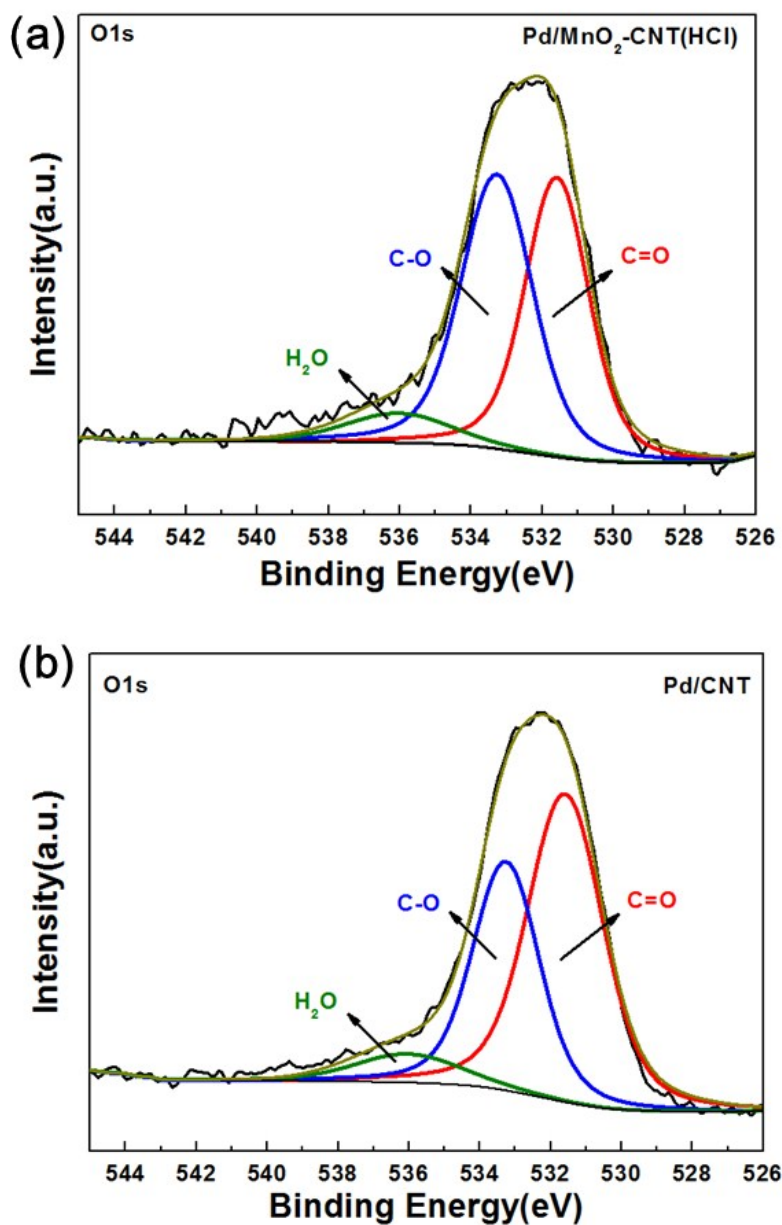


Figure S9. High resolution O 1s spectra of Pd/MnO₂-CNT(HCl) and Pd/CNT.

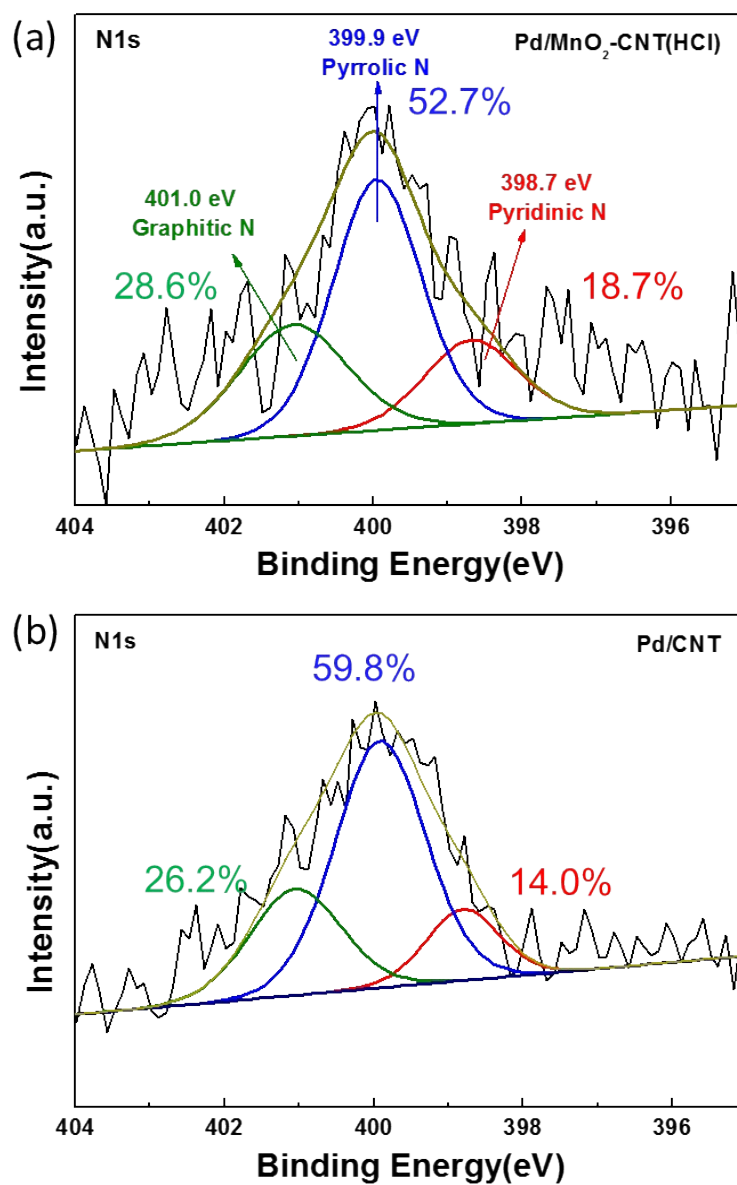


Figure S10. High resolution N 1s spectra of Pd/MnO₂-CNT(HCl) and Pd/CNT

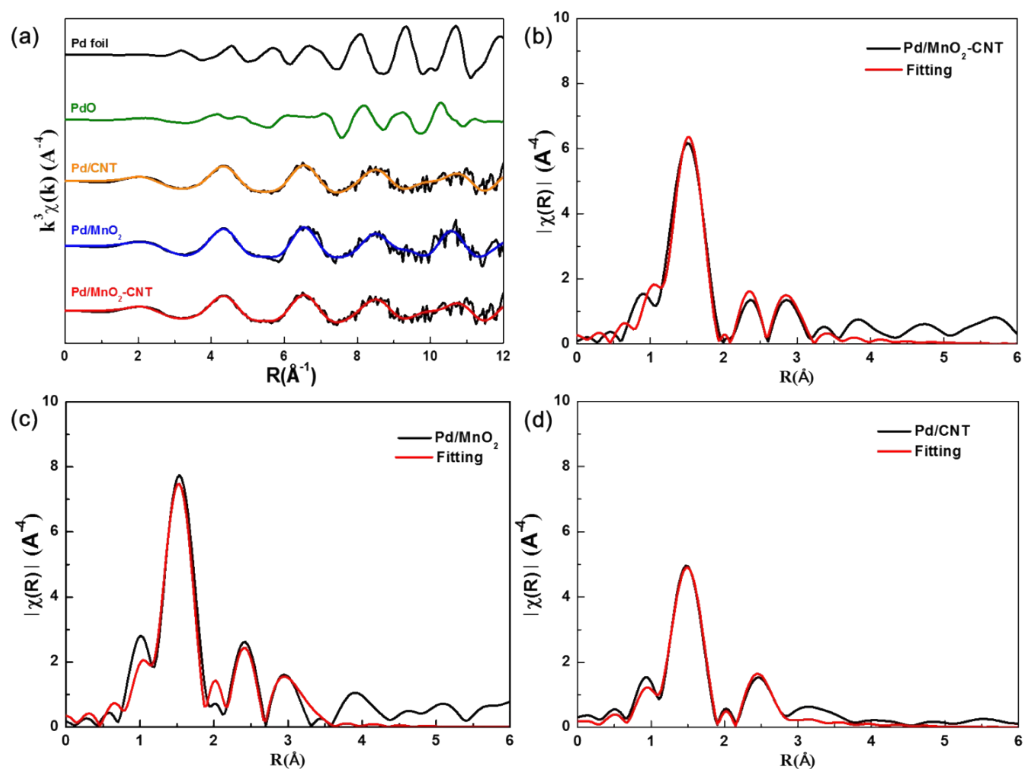


Figure S11. (a) The EXAFS oscillation functions at the Pd K-edge of PdO, Pd foil, Pd/CNT, Pd/MnO₂, Pd/MnO₂-CNT, (b, c, d) EXAFS spectra and the fitting curves of Pd/MnO₂-CNT, Pd/MnO₂ and Pd/CNT.

Table S2. Structural Parameters of PdO, Pd foil, Pd/MnO₂, Pd/CNT and Pd/MnO₂-CNT

derived from quantitative EXAFS curve-fitting using the IFEFFIT software.

Sample	Shell	CN	R	ΔE_0 (eV)	$\sigma^2(10^{-3} \text{ \AA}^2)$	R-factor
Pd/MnO₂	Pd-O-1	4.5±0.4	2.00±0.01	-1.4±1.3	2.4±1.0	0.004
	Pd-Pd	1.5±1.0	2.71±0.03	3.2±4.0	8.4±7.2	-
	Pd-Mn-1	1.5±0.6	3.00±0.04	3.2±4.0	7.0	-
	Pd-Mn-2 or	2.9±1.1	3.48±0.08	-4.4	7.0	
	Pd-O-2					
Pd/MnO₂- CNT	Pd-O-1	4.4±0.6	2.01±0.01	-1.6±2.3	3.8±1.8	0.01
	Pd-Pd	1.8±0.7	2.68±0.03	-0.7±3.0	10.0	-
	Pd-Mn-1	0.9±0.6	3.05±0.09	-0.5	5.0	-
	Pd-Mn-2 or	3.1±1.9	3.51±0.10	-0.5	13.0	
	Pd-O-2					
Pd/CNT	Pd-O-1	3.5±0.2	1.99±0.01	-6.9±1.1	3.2±0.7	0.003
	Pd-Pd	2.0±0.5	2.70±0.02	-5.8±1.8	12.3±2.5	
Pd foil	Pd-Pd	12	2.74±0.01	0.7±0.5	4.6±0.5	0.002
PdO	Pd-O	4	2.01	-	-	-
	Pd-Pd	4	3.02	-	-	-

N, coordination numbers; R, the internal atomic distance; σ^2 , Debye-Waller factor; ΔE_0 , the edge-energy shift.

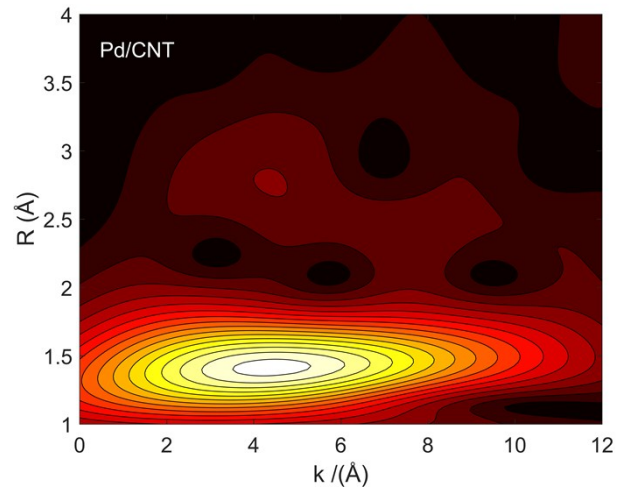


Figure S12. Full WT contour plot of Pd/CNT.

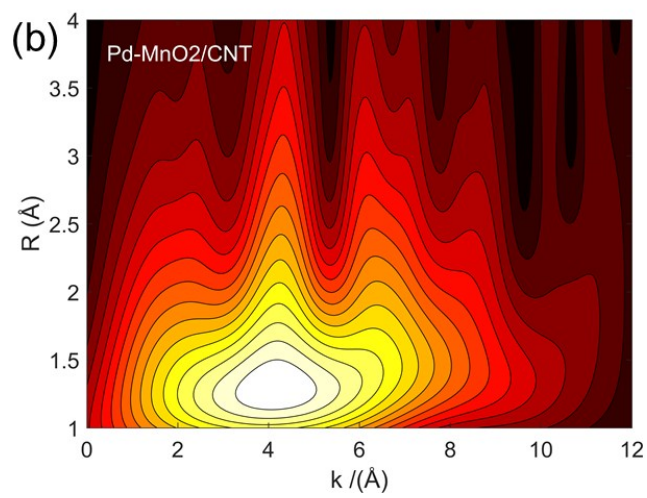
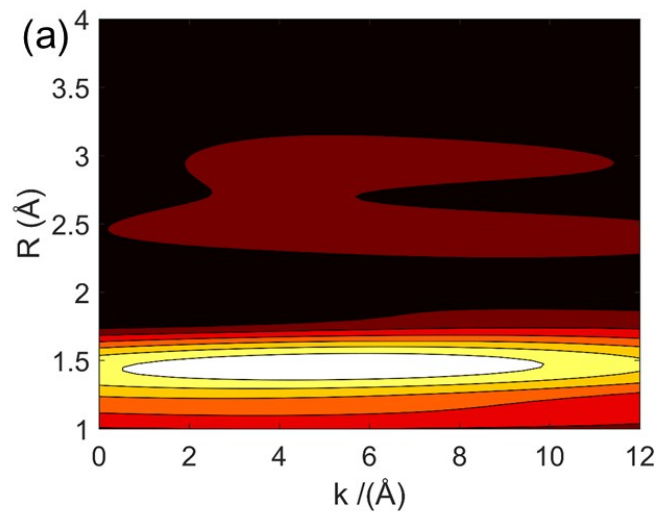


Figure S13. (a) Full WT contour plot of Pd/MnO₂ with improved resolution in R-space by applying large product of $\kappa\eta$. (b) Full WT contour plot of Pd/MnO₂ with improved resolution in k-space by applying small product of $\kappa\eta$

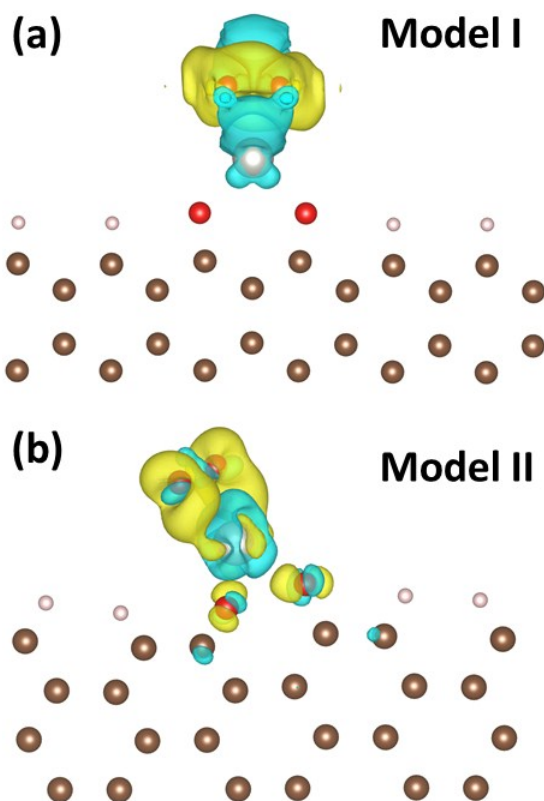


Figure S14. Top view of the charge density difference images of model I and II. Difference in charge density ($\Delta\rho$) of O₂ adsorbed on Pd-O/C with the blue and yellow areas denoting decreased and increased charge density, respectively. This contour map shows that the electrons transfer from Pd to oxygen containing fragment. The isosurface value is set as 0.05 e/Å³.

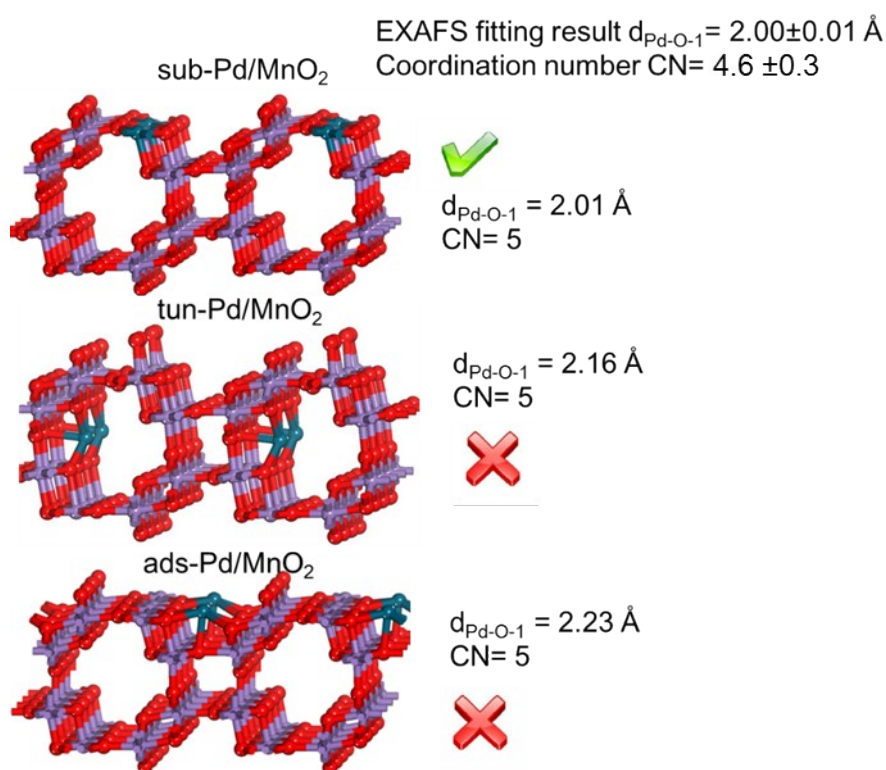


Figure S15. Geometrically optimized structures of sub-Pd/MnO₂, tun-Pd/MnO₂, and ads-Pd/MnO₂. Only the structure parameters of sub-Pd/MnO₂ agree with the EXAFS fitting results.

Table S3. Interaction energy (E^{int}), d-band center (ϵ_d), coordination number (CN), bond length of Pd-O/C (R) and bond length of adsorbed O₂ molecule ($d_{\text{O-O}}$) of a Pd atom attached to oxygen.

	Pd-O/C models			
	I	II	III	IV
E^{int} (eV)	1.69	2.33	0.96	1.08
ϵ_d (eV)	-2.12	-2.04	-1.82	-1.87
CN	4.0	4.0	4.0	4.0
R(Å)	2.006	2.016	1.988	1.986
Pd electron loss	0.78e	0.77e	0.82e	0.83e

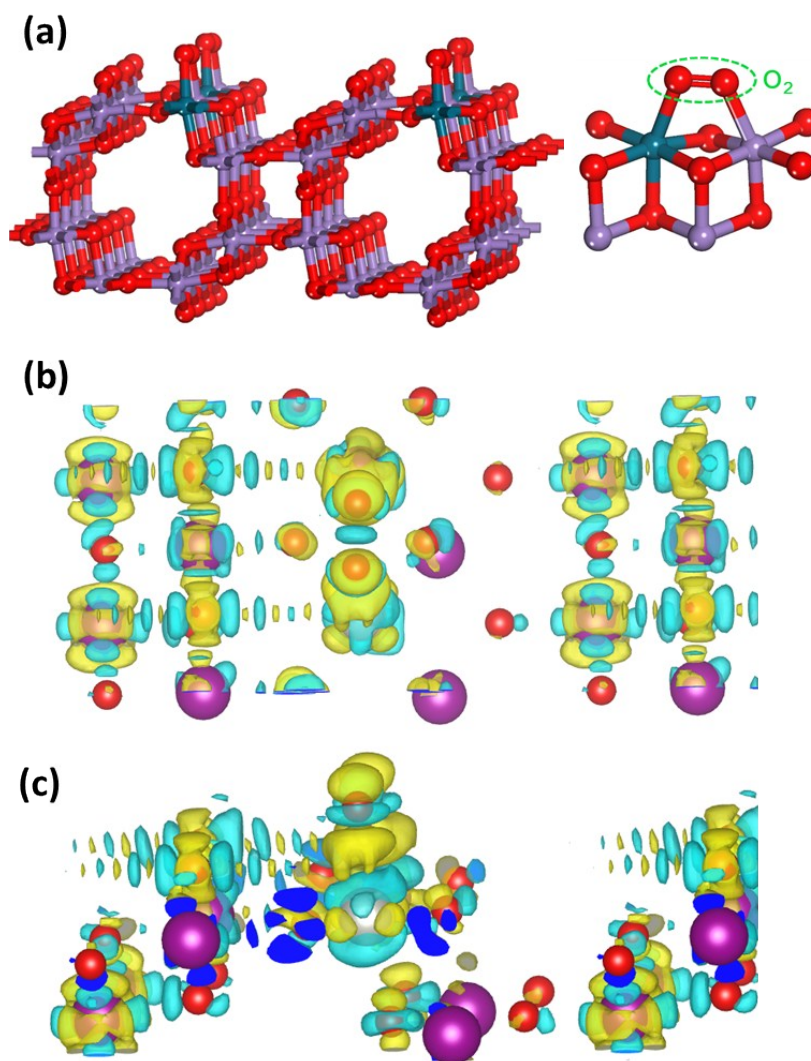


Figure S16. (a) Geometrically optimized atomic structures of O_2 adsorbed Pd/MnO₂ with E_{ads} of -0.80 eV. The dark cyan, red, and purple spheres represent Pd, O and Mn atoms respectively. (b) Corresponding top view and side view of the charge density ($\Delta\rho$) difference images of Pd/MnO₂ with the blue and yellow areas denoting decreased and increased charge density, respectively. The calculated the charge density difference (CDD) was defined as $\Delta\rho = \rho_{\text{total}} - \rho_{\text{slab}} - \rho_{\text{O}_2}$, where ρ_{total} is the charge density for the adsorbed system and ρ_{slab} and ρ_{O_2} are the charge densities for the Pd/MnO₂(100) and O₂, respectively. This contour map shows that the electrons transfer from Pd to MnO₂(100). The isosurface value is set as 0.05 e/Å³.

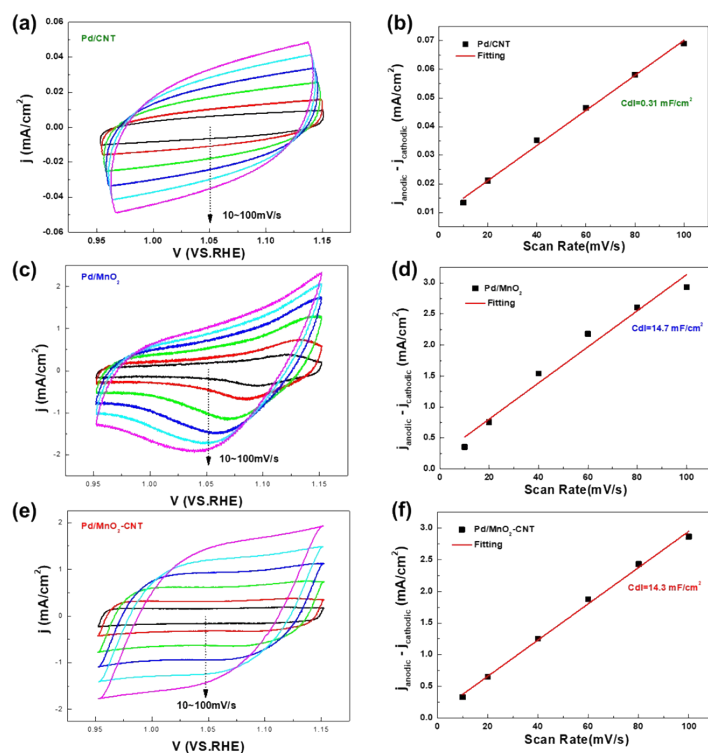


Figure S17. (a, c, e) CV curves recorded at different scanning rates (10, 20, 40, 60, 80, 100 mV/s). (b, d, f) Plots showing the extraction of the double layer capacitance (C_{dl}) for estimating electrochemical surface area (ECSA). The linear slope of capacitive current vs. scanning rate is equivalent to twice C_{dl} .

Table S4. TOF of different electrocatalysts.

Electrocatalyst	TOF (s^{-1}) @0.9V	TOF (s^{-1}) @0.8V
Pd/CNT	0.0013	0.076
Pd/MnO ₂	0.026	0.056
Pd/MnO ₂ -CNT	0.137	0.328

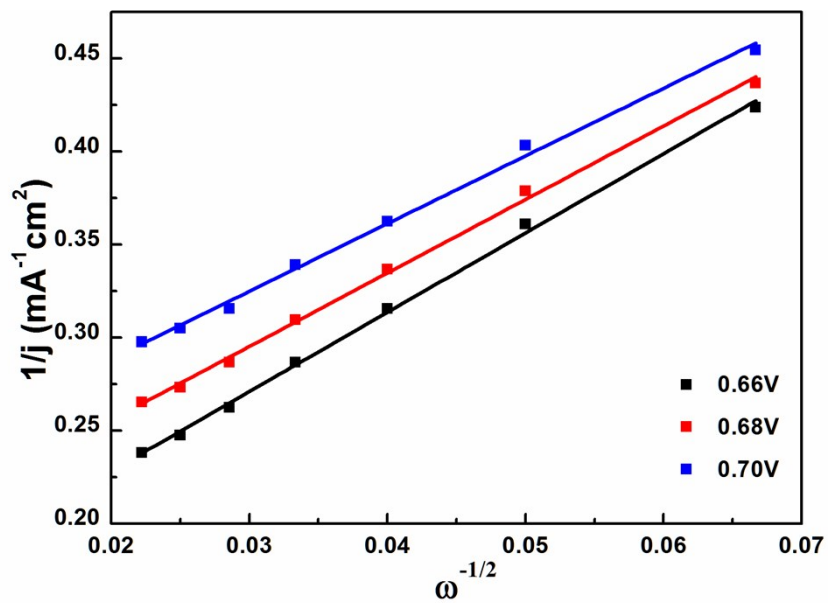


Figure S18. The K-L plots of Pd/MnO₂-CNT.

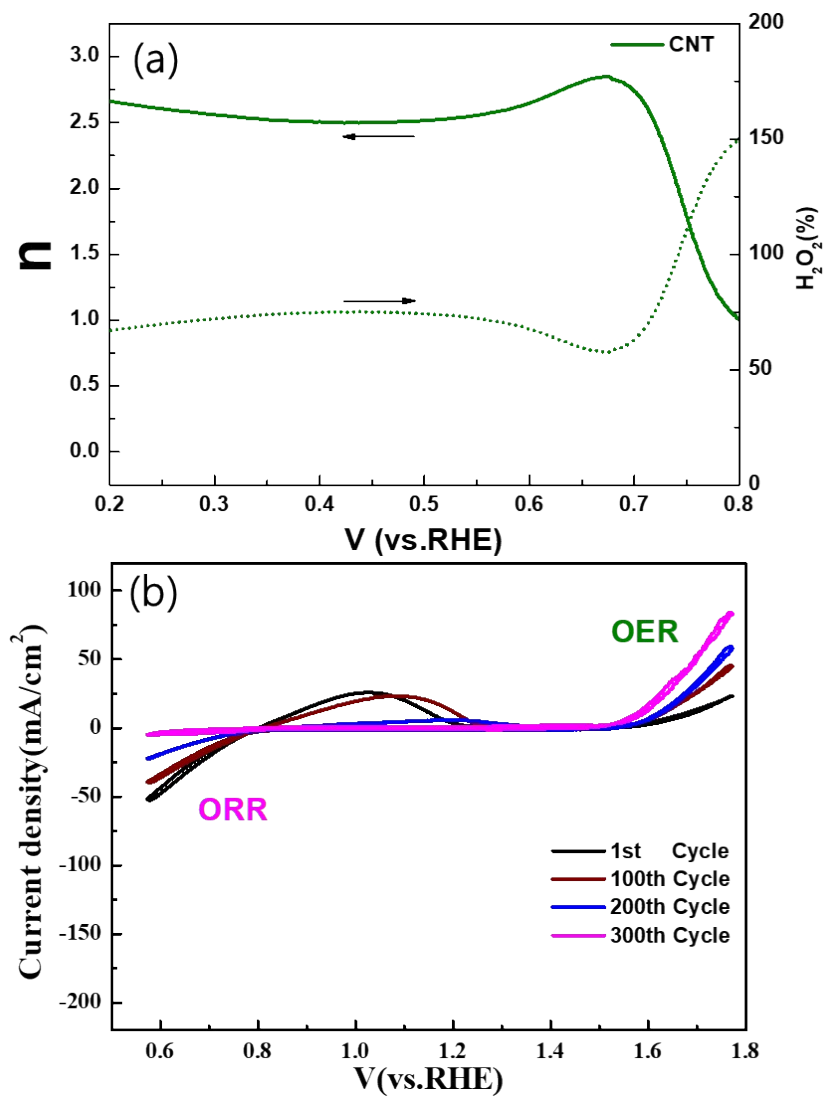


Figure S19. (a) Dependence of n and peroxide yield of CNT on the potential. (b) CV curves of CNT in O₂-saturated 6 M KOH.

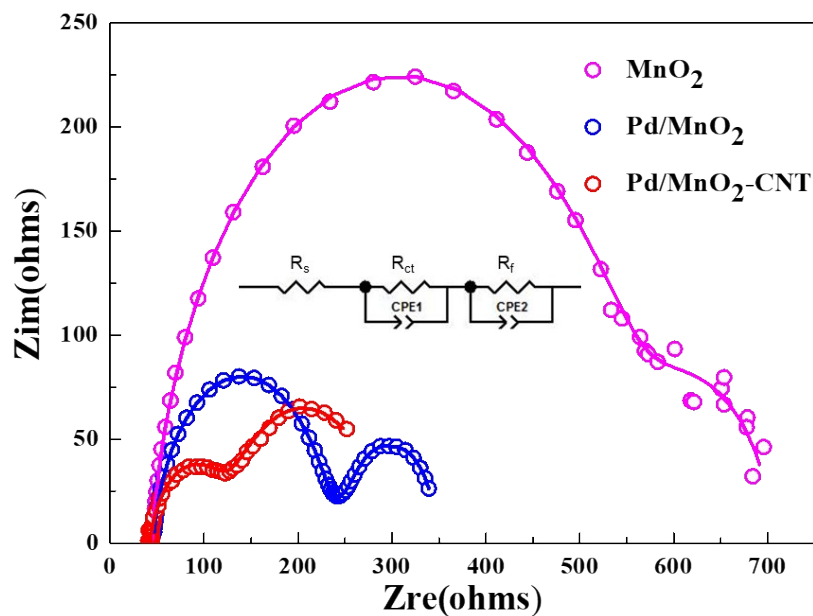


Figure S20. Nyquist plot of MnO₂, Pd/MnO₂ and Pd/MnO₂-CNT measured at a potential of 0.65 V (vs RHE). Dotted line is the experimental data, and solid line is the simulated data. The insert shows the electrical equivalent circuit. R_s, R_{ct} and R_f represent series resistance, charge transfer resistance and diffusion resistance. CPE is the constant phase element.

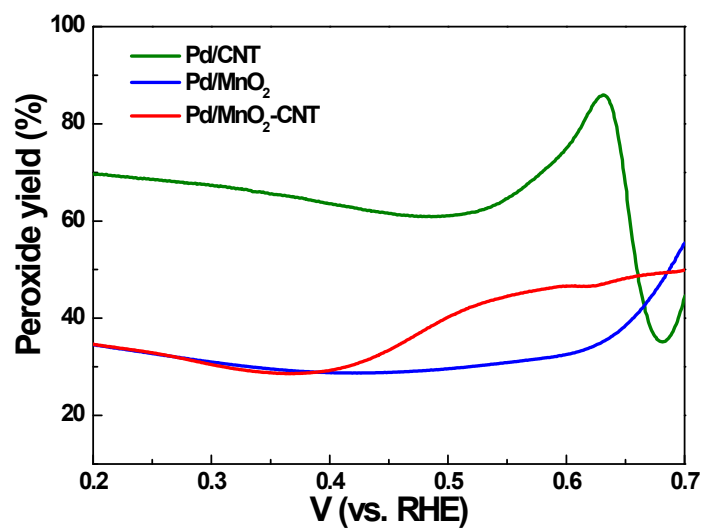


Figure S21. Peroxide yield of Pd/CNT, Pd/MnO₂ in 6 M KOH electrolyte

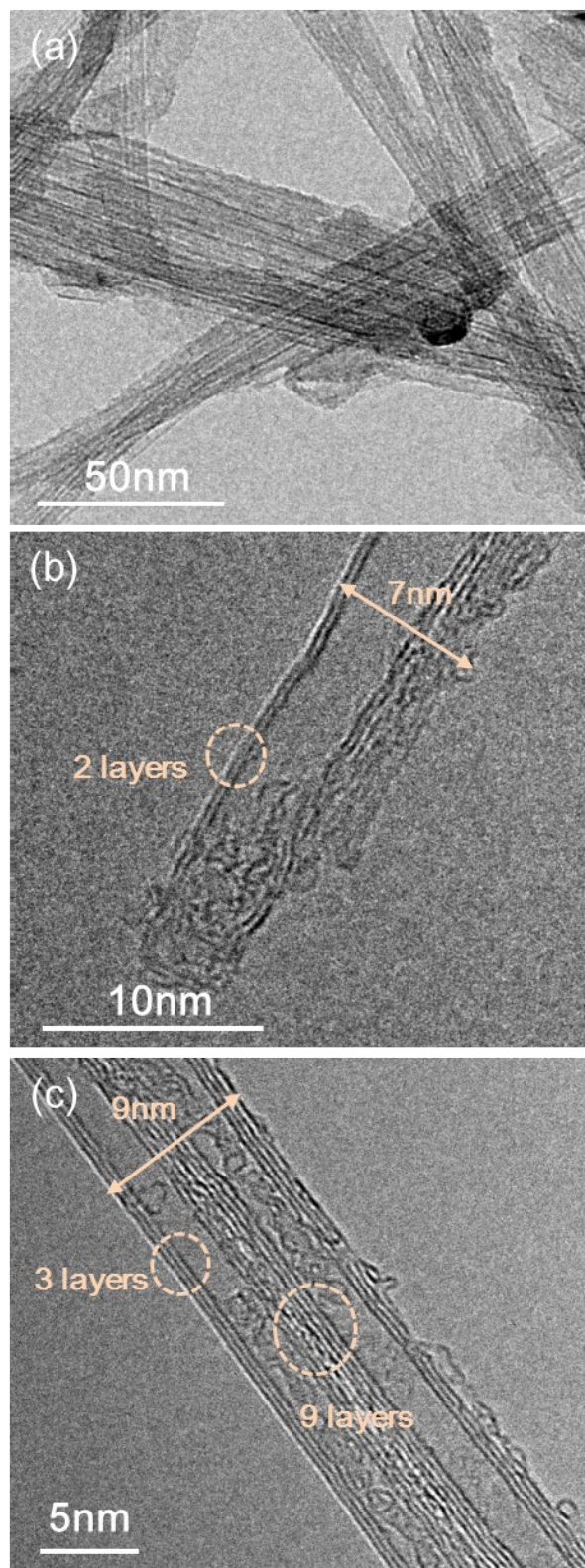


Figure S22. TEM images of Pd/CNT after cycling for 600 CV cycles.

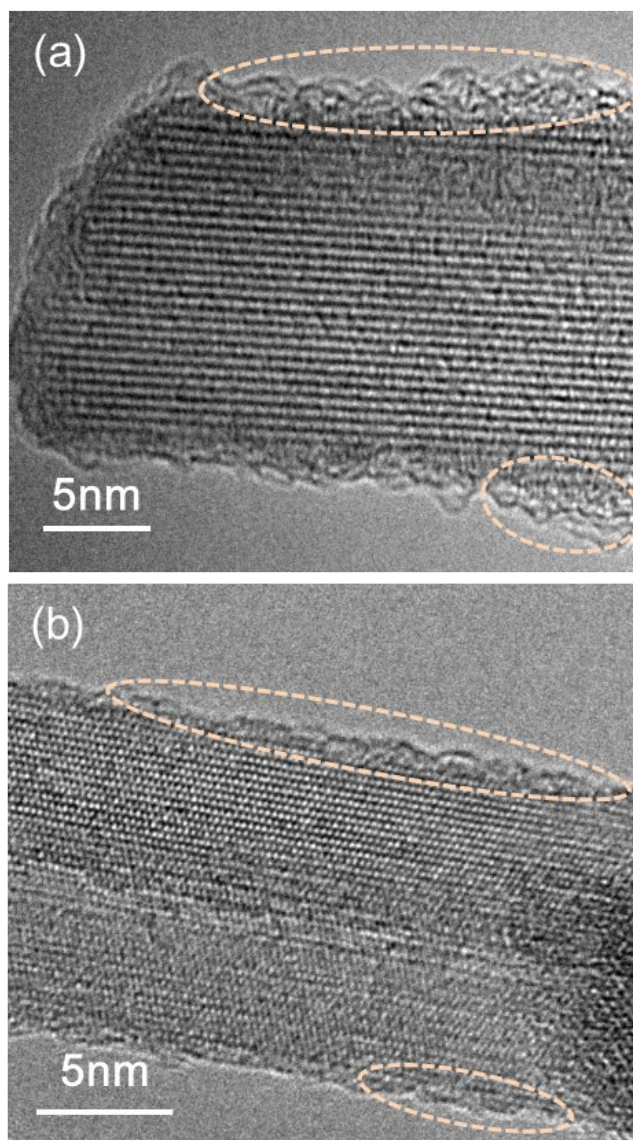


Figure S23. TEM images of (a) MnO₂ and (b) Pd/MnO₂ after cycling for 600 CV cycles.

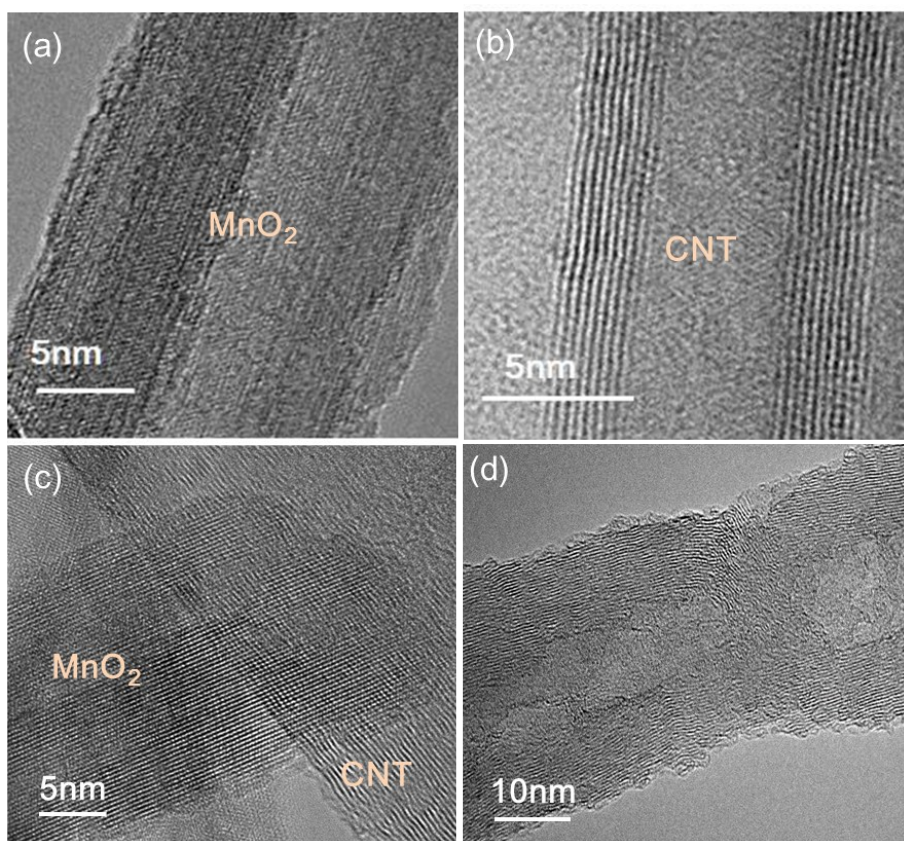


Figure S24. (a, b, c, d) TEM images of Pd/MnO₂-CNT after cycling for 600 CV cycles. d shows a CNT with large diameter with no observation of carbon corrosion.

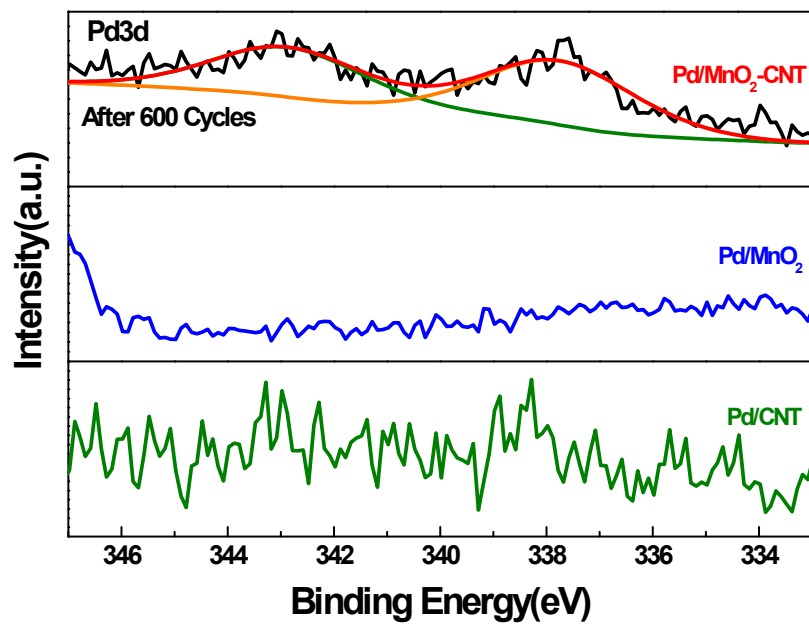


Figure S25. High resolution 3d spectra of Pd/MnO₂-CNT, Pd-MnO₂ and Pd/CNT after 600 electrochemical cycles.

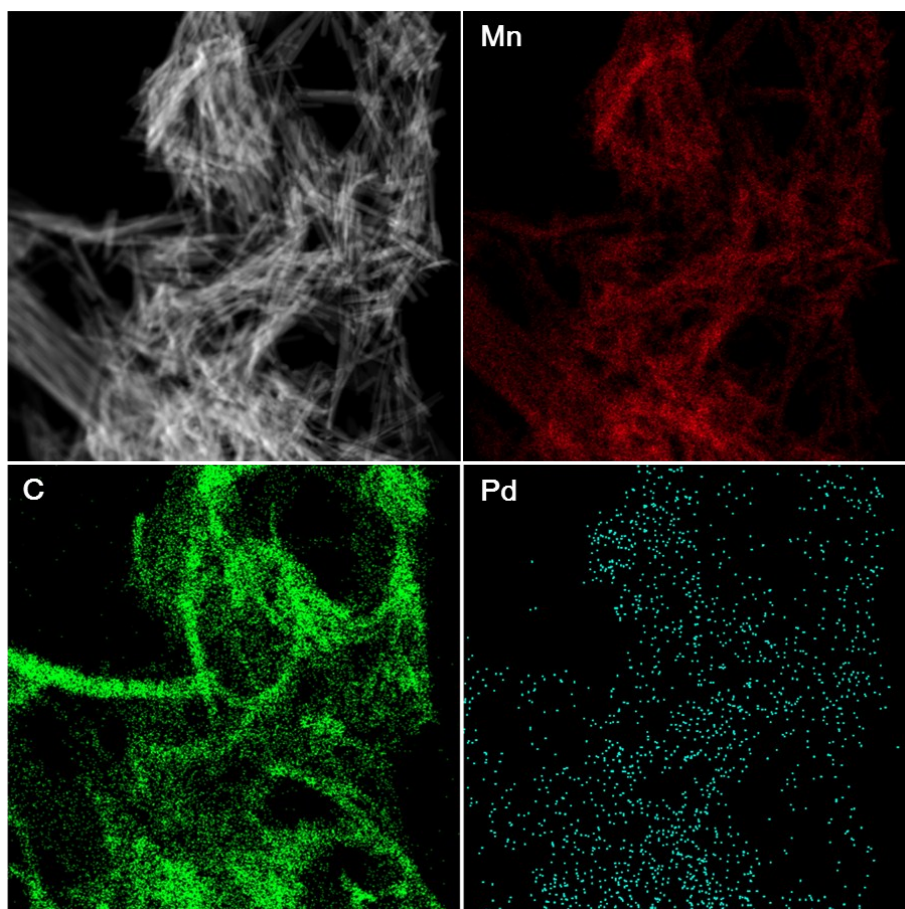


Figure S26. STEM image and the corresponding EDS mapping of Pd/MnO₂-CNT after cycling for 600 CV cycles.

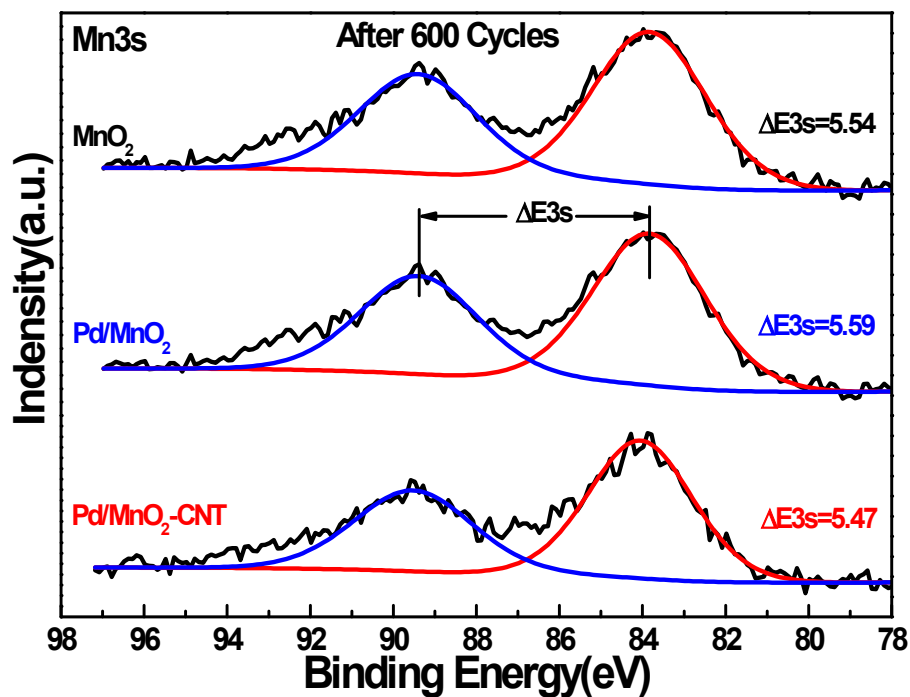


Figure S27. High resolution Mn 3s spectra of MnO₂, Pd/MnO₂, and Pd/MnO₂-CNT after cycling for 600 CV cycles.

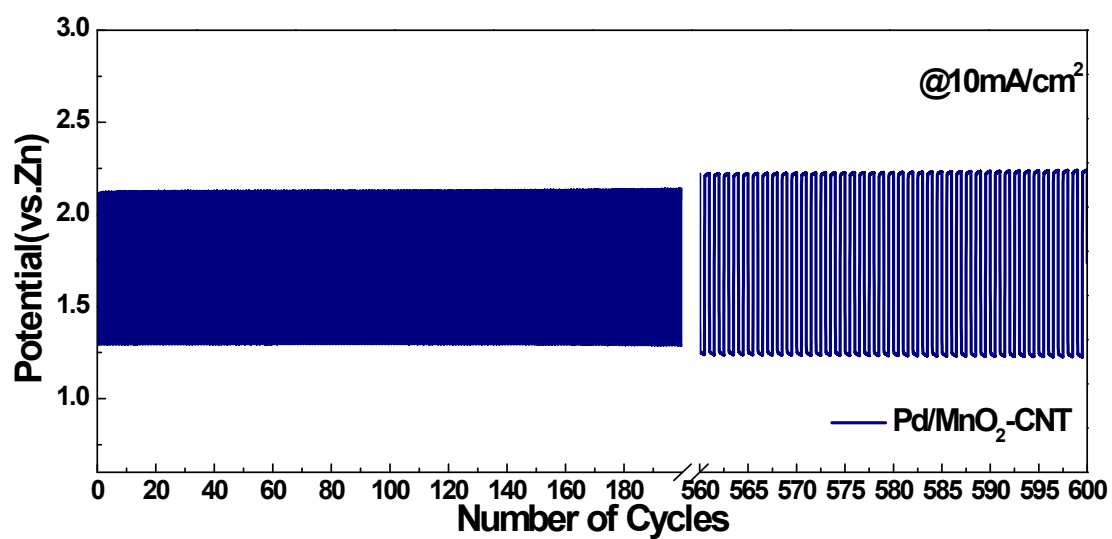


Figure S28. Cycling performance of Pd/MnO₂-CNT at a cycling current density of 10 mA cm⁻².

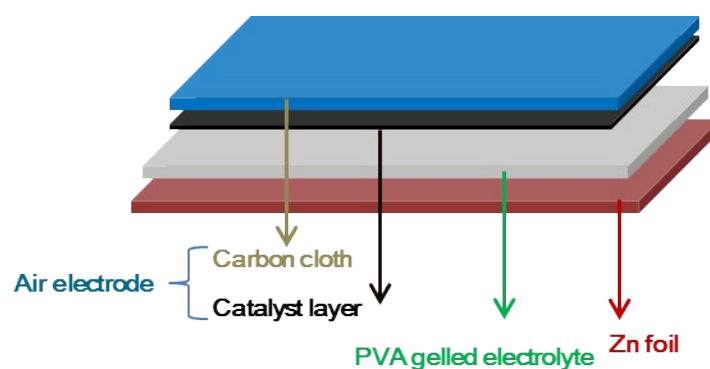


Figure S29. Schematic battery structure of SZAB.

Table S5. Comparison of the MA_{Pd} of our Pd/MnO₂-CNT with recently reported electrocatalysts in alkaline media. The MA_{Pd} was obtained by normalizing the current density at different voltage (vs. RHE) to Pd mass loading.

Entry	Catalysts	Electrolyte	Pd Size	Potential (V)	MA_{Pd} (A/g)
This Work	Pd/MnO ₂ -CNT	0.1 M KOH	Atomic dispersion	0.9	484
S14	rGO-Pd [†]	1 M KOH	~3 nm	0.9	8
S15	HDC-Pd [†]	0.1 M KOH	~13 nm	0.9	75
S16	Pd NDs [†]	0.1 M KOH	~17.5 nm	0.9	97
S17	Pd Cubes/RGN [†]	0.1 M NaOH	~10.8 nm	0.90	30
S18	Pd-CN _x [†]	0.5 M NaOH	~10.8 nm	0.90	19

†The rGO, HDC, RGN and CN_x represent reduced graphene oxide, heteroatom doped carbon, reduced graphene nanosheet and carbon nitride, respectively.

Table S6. Comparison of the stability properties of the Pd/MnO₂-NCNT with other reported Pd based electrocatalyst supported by manganese oxides and/or carbon nanomaterials.

Entry	Electrocatalyst	Targeted reaction	Electrolyte	Current density loss
This work	Pd/MnO ₂ -CNT	ORR & OER	6 M KOH	ORR – no loss after 600 cycles OER – no loss after 100 cycles 11.6% after 600 cycles
			0.1 M KOH + 0.25 M CH ₃ OH	(~3% after 5 h)
S19	Pd (nanoparticle)-MnO ₂ /MWCNT	Methanol oxidation	0.5 M NaOH + 1M CH ₃ OH	> 50% after 0.33h
S20	Pd (nanoparticle)-Mn ₃ O ₄ /MWCNT	Methanol oxidation	0.5 M NaOH + 1.0 M CH ₃ OH solution	~ 40% after 0.5h
S21	Pd(nanoparticle)/MnO ₂ -rGO†	Methanol oxidation	0.5 M KOH+1 M CH ₃ OH	~75% after 0.5 h
S22	MnO ₂ -Pd (nanoparticle)/OLC†	Glycerol oxidation	0.5 M KOH + 0.5 M Glycerol	~72% after 0.33 h
S23	Pd/CNO†	Formaldehyde oxidation	0.1 M NaOH + 0.3 M HCOH	~34% after 150 cycles
S24	Pd (nanoparticle)/C	ORR	0.1 M NaOH	18% after 0.55 h
S25	Pd(nanoparticle)/MWCNT	ORR	0.1 M NaOH	~18% ECSA loss after 600 cycles‡
S26	Pd cubes/RGN†	ORR	0.1 M NaOH	~14% after 500 cycles
S27	PdO/C	ORR	0.1 M NaOH	~52% ECSA loss after 2000 cycles‡

†The rGO, OLC, CNO and RGN, represent reduced graphene oxide, onion like carbon, carbon nanooions, and reduced graphene nanosheet, respectively. ‡ECSA means electrochemical surface area.

Supporting References

- [S1] J. W. Elam, A. Zinovev, C. Y. Han, H. H. Wang, U. Welp, J. N. Hryn, M. J. Pellin, *Thin Solid Films* 2016, **515**, 1664.
- [S2] J. Lu, P. C. Stair, *Langmuir* 2010, **26**, 16486.
- [S3] H. Funke, M. Chukalina, A. C. Scheinost, *J. Synchrotron Rad.* 2007, **14**, 426.
- [S4] B. Y. Hong, J. Miao, S. F. Hung, J. Chen, H. B. Tao, X. Wang, L. Zhang, R. Chen, J. Gao, H.M. Chen, L. Dai, B. Liu, *Sci. Adv.* 2016, **2**, e1501122.
- [S5] P.E. Blöchl, *Phys. Rev. B* 1994, **50**, 17953.
- [S6] J. P. Perdew, K. Burke, M. Ernzerhof, *Phys. Rev. Lett.* 1996, **77**, 3865.
- [S7] G. Kresse, J. Hafner, *Phys. Rev. B* 1993, **47**, 558.
- [S8] G. Kresse, J. Furthmüller, *Phys. Rev. B* 1996, **54**, 11169.
- [S9] S. L. Dudarev, G. A. Botton, S. Y. Savrasov, C. J. Humphreys, A. P. Sutton, *Phys. Rev. B* 1998, **57**, 1505.
- [S10] E. Cockayne, L. Li, *Chem. Phys. Lett.* 2012, **544**, 53-58.
- [S11] H. J. Monkhorst, J. D. Pack, *Phys. Rev. B* 1976, **13**, 5188-5192.
- [S12] W. L. Yim, Z. F. Liu, *Chem. Phys. Lett.* 2004, **398**, 297.
- [S13] H. Xu, D. Cheng, D. Cao, X. Zeng, *Nat. Catal.* 2018, **1**, 339-348.
- [S14] Y. X. Huang, J. F. Xie, X. Zhang, L. Xiong, H. Q. Yu, *ACS Appl. Mater. Interfaces* 2014, **6**, 15795.
- [S15] L. Xiong, J. J. Chen, Y. X. Huang, W. W. Li, J. F. Xie, H. Q. Yu, *Nano Energy* 2015, **12**, 33.
- [S16] Q. Gao, M. R. Gao, J. W. Liu, M. Y. Chen, C. H. Cui, H. H. Li, S. H. Yu, *Nanoscale* 2013, **5**, 3202.
- [S17] Z. T. Liu, K. L. Huang, Y. S. Wu, Y. P. Lyu, and C. L. Lee, *Electrochim. Acta* 2015, **186**, 552-561.
- [S18] T. Bhowmik, M. K. Kundu, S. Barman, *Int. J. Hydrogen Energy* 2016, **41**, 14768.
- [S19] Y. Zhao, L. Zhan, J. Tian, S. Nie, Z. Ning, *Int. J. Hydrogen Energy* 2010, **35**, 10522.
- [S20] Y. Zhao, S. Nie, H. Wang, J. Tian, Z. Ning, X. Li, *J. Power Sources* 2012, **218**, 320.
- [S21] R. Liu, H. Zhou, J. Liu, Y. Yao, Z. Huang, C. Fu, Y. P. Kuang, *Electrochem. Commun.* 2013, **26**, 63.
- [S22] H. Bao, X. Sun, Z. Jiang, Y. Huang, J. Wang, *Chinese J. Cata.* 2014, **35**, 1418-1427.
- [S23] A. Shaikh, S. Parida, *RSC Adv.* **2016**, **6**, 83711.
- [S24] Y. H. Xue, L. Zhang, W. J. Zhou, S. H. Chan, *Int. J. Hydrogen Energy* 2014, **39**, 8449.
- [S25] C. A. Martins, P. S. Fernández, F. de Lima, H. E. Troiani, M. E. Martins, A. Arenillas, G. Maia, G. A. Camara, *Nano Energy* 2014, **9**, 142.
- [S26] Z. T. Liu, K. L. Huang, Y. S. Wu, Y. P. Lyu, C. L. Lee, *Electrochim. Acta* 2015, **186**, 552.
- [S27] Q. Wu, Z. Rao, L. Yuan, L. Jiang, G. Sun, J. Ruan, Z. Zhou, S. Sang, *Electrochim. Acta* 2014, **150**, 157.